Science of Sintering, **50** (2018) 95-109

doi: https://doi.org/10.2298/SOS1801095M

UDK 661.143; 622.785

Structural, Morphological and Electrical Properties of Multi-Doped Calcium Phosphate Materials as Solid Electrolytes for Intermediate Temperature Solid Oxide Fuel Cells

Miljana Mirković[1*)], Anja Dosen[1], Suzana Erić[2], Marija Stojmenović[1], Branko Matović[1], Aleksandra Rosić[2]

[1]Institute of Nuclear Sciences "Vinča", University of Belgrade, Mihaila Petrovića Alasa 12–14, 11001 Belgrade, Serbia

[2]Faculty of Mining and Geology, University of Belgrade, Đušina 7, 11001 Belgrade, Serbia

Abstract:

Modified solution precipitation method was used to prepare pure and doped Mg, Sr and Na hydroxyapatite type materials (CaP, CaMgP and CaSrNaP). Modification consisted of partial substitution of nitrates by acetate solution in order to achieve a more soluble and cost effective synthesis. The obtained samples were calcined at 400 ºC (CaP_{400}, $CaMgP_{400}$ and $CaSrNaP_{400}$). All powders were characterized by X-ray diffraction (XRD), Fourier transform infrared (FTIR) spectroscopy and scanning electron microscopy (SEM). Calcined samples were densified at 1000 ºC in an air for 3 h (CaP_{1000}, $CaMgP_{1000}$ and $CaSrNaP_{1000}$). Sintered samples were characterized by XRPD, FTIR, SEM, EDS and complex impedance methods. The highest conductivity was found for the multi-doped phosphate sample ($CaSrNaP_{1000}$) at 700 ºC ($1.90\times10^{-3}\Omega^{-1}cm^{-1}$). The corresponding activation energies of conductivity amounted to 0.31 eV in the temperature range 500-700 ºC.

Keywords: *Sintering; X–ray diffraction; Electrical conductivity; Phosphate materials; Fuel cells.*

1. Introduction

Due to the high efficiency and applicability of different types of fuels (biogas, natural gas, hydrogen and methane) [1-4], Intermediate Temperature Solid Oxide Fuel Cells (IT–SOFCs) have become one of the most promising energy conversion devices and emphasis is placed on the development of micro–SOFCs as power sources [5], which could operate at reduced temperatures in porTab. electronic devices. To achieve this goal, it is necessary to synthesize material with corresponding properties. Generally, the conductivity of these systems depends on the processing and intrinsic properties of the material itself, where micro structural features and density have a key role [6]. Recently, cerium (IV) oxide (CeO_2) solid solution materials became favored for potential use in IT–SOFCs, with appropriate doping methods may create fluorite–type crystal lattice which has a good influence at ionic conductivity but the use of CeO_2 and oxide rare–earth is very expensive [7-10]. An adequate substitute for CeO_2 might be calcium phosphate hydroxyapatite HA ceramics - $Ca_5(PO_4)_3OH$, due to their physical and chemical properties and very low cost of synthesis [11, 12]. Various types of synthesis were used for preparation HA ceramics: sol–gel processes [13],

*) **Corresponding author:** miljanam@vinca.rs

hydrothermal synthesis [14] and solid state reaction method [15]. In comparison to these methods, direct precipitation from aqueous solution provides an easier way of preparing HA ceramic and at the same time provides a large amount high purity material [16-18].

Furthermore, ion substituted calcium phosphate materials can be prepared using simple chemical precipitation method, which is of great importance when it comes to obtaining a solid ionic conductor for use in IT–SOFCs, the advantages of this method include simple synthesis, low cost and ability to obtain large quantity and high purity of solid electrolyte [18].

In recent years, ionic substitutions of Mg^{2+}, Na^{+} and Sr^{2+} in HA [11, 12] proved very interesting for their potential implementation in IT–SOFCs, owing to the morphology, thermal stability, and structural and mechanical properties [19]. Low–temperature treatment (400–500 ºC) allows preserving the particle morphology and developing nanoscale structures i.e. grains [20, 21]. In order to obtain compact material densification process usually requires sintering at temperatures at or above 1000 ºC, however, this leads to the formation of high temperature calcium phosphate ceramics [22-24]. Knowledge of thermal stability, ionic transport properties and possible mechanisms of conduction properties of different calcium phosphate materials provides a key for their application in IT–SOFCs [11, 12]. In this study, we show Mg^{2+}, Na^{+} and Sr^{2+} HA materials as suiTab. candidates for ionic conductive materials. Materials were treated thermally in air atmosphere at 400 ºC (CaP_{400}, $MgCaP_{400}$ and $NaSrCaP_{400}$). Additionally, behavior doped CaP after sintering at 1000 ºC during 3 h (CaP_{1000}, $MgCaP_{1000}$ and $NaSrCaP_{1000}$) was studied. The main objective was to obtain a range of dense solid solution calcium phosphate materials, with suiTab. morphology and grain size for the application in Intermediate Temperature Solid Oxide Fuel Cells.

2. Material and methods

2.1. Synthesis of CaP, CaMgP and CaSrNaP samples

Samples were prepared by solution precipitation method. Pure hydroxyapatite (CaP) was prepared by drop wise addition of 250 ml 0.3 M NaH_2PO_4+H_2O into 250 ml $Ca(OH)_2$, 0.5 M solution which was magnetically stirred. The pH was adjusted to 11 using NH_4OH, at temperature about 100 ºC. To synthesize Mg (CaMgP) and NaSr (NaSrCaP) substituted hydroxyapatite materials we used slightly modified precipitation method. To obtain MgHA, 250 ml NaH_2PO_4+H_2O, 0.3 M was heated at 100 ºC and added drop wise into mechanically stirred mixture of 250 ml $Ca(OH)_2$, 0.5 M and 250 ml $MgCl_2{\cdot}6H_2O$, 0.25 M heated to about 100 ºC, pH was adjusted to 12 using NH_4OH solution. For NaSrCaP synthesis, mixture of 250 ml of $(CH_3COOH)_2Ca{\cdot}H_2O$, 0.03 M and 250 ml $Sr(CH_3COO)_2$, 0.03 M was added drop wise into 500 ml NaH_2PO_4+H_2O, 0.3 M at room temperature. The precipitates were washed, centrifuged at 3000 rpm and dried at 70 ºC for 17 h. Dry powders were thermally treated at 400 ºC during 3h in air atmosphere, and then uniaxially pressed at 105 MPa into compact pelets (8 mm diameter), and sintered at 1000 ºC for 3 h in air atmosphere.

2.2. Densification of CaP, CaMgP and CaSrNaP samples

Samples were uniaxially pressed at 105 MPa and thermally treated. Sample annealing was carried out at 1000 ºC for 3 h in an air at a heating rate of 5 ºC/min. The resulting density was determined via Archimedes' method. Densified samples were characterized using X-ray diffraction (XRD), scanning electron microscopy (SEM), Energy Dispersive Spectroscopy (EDS) and complex impedance methods.

2.3. Characterization of CaP, CaMgP and CaSrNaP samples

Phase composition before and after thermal treatment as well as crystallite size evolution were analyzed by X-ray diffraction (XRD) using Ultima IV Rigaku diffractometer, equipped with CuKα radiation, using a generator voltage 40.0 kV and a generator current 40.0 mA. The range of 5–80° 2θ was used in a continuous scan mode with a scanning step size of 0.02° and count time 2°/min. Analysis was done using PDXL2 software (version 2.0.3.0) [25], with reference to ICDD database [26]. For quantitative phase analysis, RIR method was used. Structural modeling was done using VESTA program [27]. Spectroscopic studies of the synthesized and thermally treated materials were carried out in the mid infrared (MIR) regions (4000–400 cm^{-1}) using Fourier transforms infrared (FTIR) spectroscopy, in transmission mode by a Perkin Elmer Spectrum Two FT-IR spectrometer using the pressed KBr compacts (1:100) technique.

The morphology and chemical composition of samples were identified using a JEOL JSM-6610LV Scanning Electron Microscope with an X-Max Energy Dispersive Spectrometer. Samples were coated with gold using a BALTEC-SCD-005 sputter coating device, and the results were recorded under high vacuum conditions. The electrical conductivity of sintered samples was measured by complex impedance method, in a frequency range 1 Hz-0.1 MHz, using Interface 1000 Potentiostat/ Galvanostat/ ZRA and EIS300 Electrochemical Impedance Spectroscopy Software. The measurements were conducted in air, in the temperature range 500-700 ºC, with a 50 ºC increment. The amplitude of the applied sinusoidal voltage signal was 20 mV. Thin layer of high conductivity silver paste was applied onto both sides of the sample pellets in order to provide good electrical contact between electrolyte and electrodes. The samples were placed between the silver plates in a ceramic holder which was heated by vertical oven. A Pt–Rh thermocouple located just below the bottom silver plate was used for temperature monitoring. The impedance plots obtained experimentally were fitted by means of the software ZViews for Windows (Version 3.2b). The resistance values were determined from the impedance diagrams recorded at various temperatures. The specific conductance was calculated from the resistance data using the dimensions of the sample pellets.

3. Results and discussion

3.1. Structural and morphological properties of CaP, CaMgP and CaSrNaP samples

3.1.1. XRD analysis

X-Ray diffraction patterns of synthesized pure hydroxyapatite (CaP) powders, calcined at 400 ºC (CaP_{400}) and sintered at 1000 ºC (CaP_{1000}) during 3 h, are shown in Fig. 1. CaP powder shows broad peaks typical for hydroxyapatite obtained by precipitation method. CaP and CaP_{400} crystallized as hexagonal $Ca_5(PO_4)_3OH$ s.g. *P6₃/m*, (ICDD: 01-071-5048). XRD results show the formation of another calcium phosphate phase in the sintered CaP_{1000} sample. Based on peak identification, structural refinement and decomposition calculation using PDXL2 software we found that CaP_{1000} consists of 85 % β - $Ca_2P_2O_7$ (ICDD: 01-071-2123) phase and of 15 % hydroxylapatite phase (ICDD: 01-071-5048).

XRD diffraction patterns of Mg doped HA are shown in Fig. 2. Analyses show almost identical patterns as pure HA powder, however, peaks are shifted compared to pure HA material (Fig. 1), suggesting that Mg^{2+} cations were incorporated in the structure during thermal treatment at 400°C. XRD of $CaMgP_{1000}$ sample shows that heating to 1000 ºC leads to the formation of high temperature magnesium phosphate phases $Mg_2P_2O_7$ (ICDD: 00-008-0038, marked as open circles) and β-$Ca_2P_2O_7$ (ICDD: 01-071-2123, marked as solid circles).

It is evident that addition of magnesium to the HA structure leads to the formation of high temperature solid solution that includes high temperature CaMgP phases and hydroxyapatite. $CaMgP_{100}$ nominal phase composition calculated using PDXL2 software showed 55 % β-$Ca_2P_2O_7$, 30 % $Mg_2P_2O_7$ and 15 % hydroxyapatite phase.

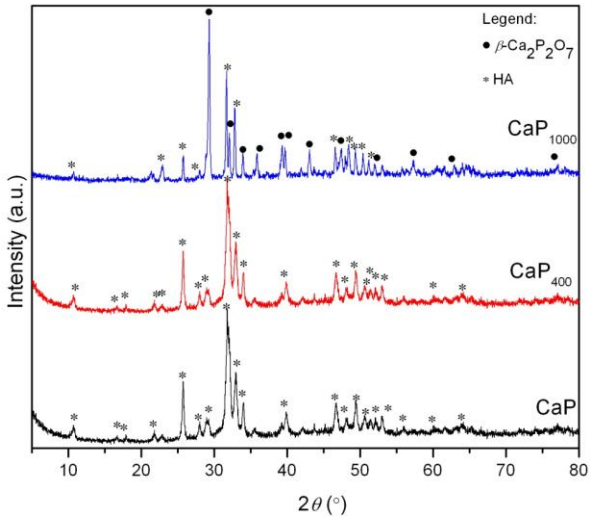

Fig. 1. XRD patterns of CaP–hydroxyapatite synthesized sample, CaP_{400}–hydroxyapatite calcinated at 400 ºC for 3 h in air, and CaP_{1000}–sintered at 1000 ºC for 3 h in air.

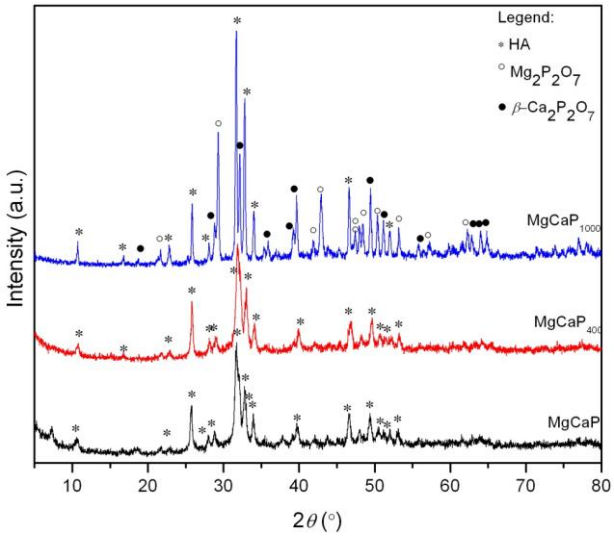

Fig. 2. XRD patterns of CaMgP–synthesized sample, $CaMgP_{400}$–calcined at 400 ºC for 3 h in air, and $CaMgP_{1000}$–sintered at 1000 ºC for 3 h in air.

The diffraction pattern of powder CaSrNaP (Fig. 3) reveals that the dried precipitate exhibits poor crystallinity, peaks around 10º and 18° 2θ (marked as inverted triangles) indicate secondary phase with chemical composition $Sr_3(P_3O_9)_2(H_2O)_7$ (ICDD:01-070-0007). The secondary phase existence is common during precipitation method of nano material synthesis [28]. However, there is no evidence of the existence of secondary phase in thermally treated $CaSrNaP_{400}$ (Fig. 3). CaSrNaP XRD peaks are slightly shifted to the left implying a larger unit cell most likely due to the incorporation of Sr into the HA lattice (Fig. 3). Thermal treatment of hydroxylapatite materials below 700 ºC leads to surface reduction and single phase particle coalescence without densification [24, 29]. At 1000 °C, high temperature solid solution forms noted as $CaSrNaP_{1000}$. Sintering at this temperature, with retention time of 3 h, high

temperature calcium, and strontium and sodium phosphate materials developed. It is evident that peaks belongs to three different phosphate phases: β – $Ca_2P_2O_7$ (01-071-2123) α-$Sr_2P_2O_7$ (ICDD: 01-072-149) and $Na_4P_2O_7$ (ICDD: 01-073-5982). Strontium and sodium phosphate phases are orthorhombic while the calcium phosphate phase is tetragonal. Structural changes and phase transitions during sintering (temperatures above 700 °C) can be explained by the loss of hydroxyl ions from the hydroxyapatite structure at temperatures around and higher than 1000 °C and the formation of orthorhombic and tetragonal phosphate phases [24, 30]. The peaks on XRD diagram are narrow and well defined indicating high structural arrangement of sintered material.

Quantitative phase analysis of CaSrNaP material showed 74% of α-$Sr_2P_2O_7$, 16% of β – $Ca_2P_2O_7$ and 10% of $Na_4P_2O_7$. Hydroxylapatite is still evident at high temperatures in the case of pure HA and HA doped with Mg. On the other hand, in the case high temperature treatment (1000 °C for 3h) of multi-doped HA leads to the formation of mixed CaSrNaP phase, with high structural arrangement.

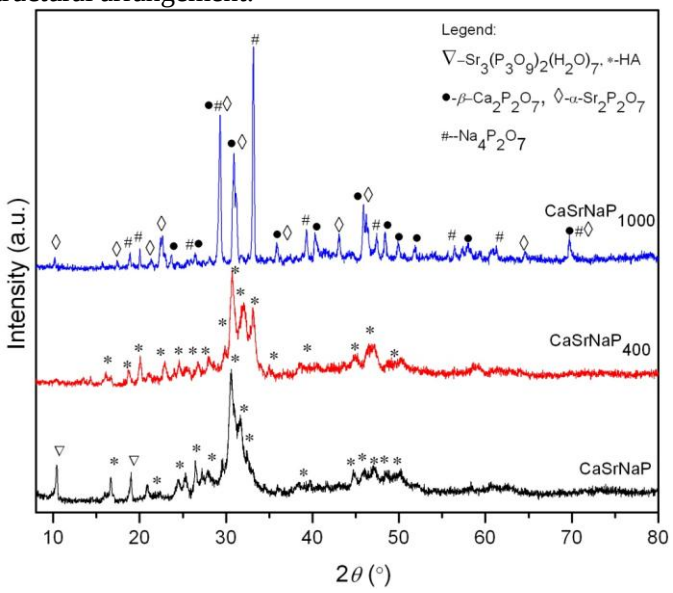

Fig. 3. XRD patterns of CaSrNaP–synthesized sample, $CaSrNaP_{400}$–calcined at 400 ºC for 3 h in air, and $CaSrNaP_{1000}$–sintered at 1000 ºC for 3 h in air.

Tab. I Unit cell parameters and crystallite sizes of obtained materials.

Samples	**Cell parameter (Å)**		**Crystallite size (nm)**
	a	***c***	
CaP	9.38(14)	6.92(19)	14(13)
CaP_{400}	9.39(10)	6.91(12)	15.2(5)
CaMgP	9.40(4)	6.87(5)	7.2(10)
$CaMgP_{400}$	9.35(3)	6.88(3)	15.6(9)
CaSrNaP	9.34(4)	6.79(4)	4.3(5)
$CaSrNaP_{400}$	9.45(6)	7.29(7)	7.9(14)

Tab. I shows variation of lattice parameters due to structural substitution during precipitation and calcinations at 400 °C. Unit cell parameters and crystallite size calculations of were performed using cif. files from American Mineralogist Crystal Data Structure Base (AMCDSB)[31] (Tab. I).

There is no significant difference in the average crystallite size of CaP and CaP_{400} samples (Tab. I). Unit cell parameters of both samples are in similar to pure hydroxyapatite (ICDD: 01-071-5048). With the increase of temperature unit cell parameter *a* increases while the parameter *c* decreases. Average crystallite size of CaMgP material increasing with temperature, which is consistent with peak shapes of obtained material. The unit cell parameters of CaMgP are higher than of CaP material, which is in correlation with published data [32]. Average crystallite size of thermally treated samples is slightly higher than synthesized. Factors that influence peak broadening are the presence of amorphous phase during precipitation and a number of dislocations between crystallite boundaries [16, 33]. During calcination at 400 ºC the material becomes crystalline and thermodynamically sTab. allowing for better arrangement and growth of crystallites [34]. The unit cell parameters of CaSrNaP and $CaSrNaP_{1000}$ have the highest value out of all examined materials, as the ionic radii of Sr^{2+} (1.13 Å) and Na^{+} (1.52 Å) are larger than ionic radii Ca^{2+} (0.99 Å) and Mg^{2+} (0.69 Å). Anisotropic change in unit cell dimensions could be attributed to the replacement of Ca^{2+} with other cations, i.e. Mg^{2+}, Na^{+} and Sr^{2+} in structure [35, 36].

3.1.2. FTIR analysis

FTIR spectra of untreated (synthesized) samples: CaP, CaMgP and CaSrNaP (Fig. 4) showed the presence of characteristic apatite signals (around: 563, 610, 657, 1030, 1077 cm^{-1}) Fig. 4b [36]. The absorbed water band is around 3500 cm^{-1}, and the band at 1413 corresponds to CO_3^{2-} group vibration [18]. In comparison with FTIR of stoichiometric HA, bands of CaSrNaP and CaMgP are red-shifted because of the presence of foreign ions incorporated into the structure [37-39]. Absence of the 631 cm^{-1} band that belongs to vibration modes of the apatitic OH groups in all tree spectra most likely indicates a lack of hydroxyl content and a possible substitution of hydroxyl groups by carbonate groups [37].

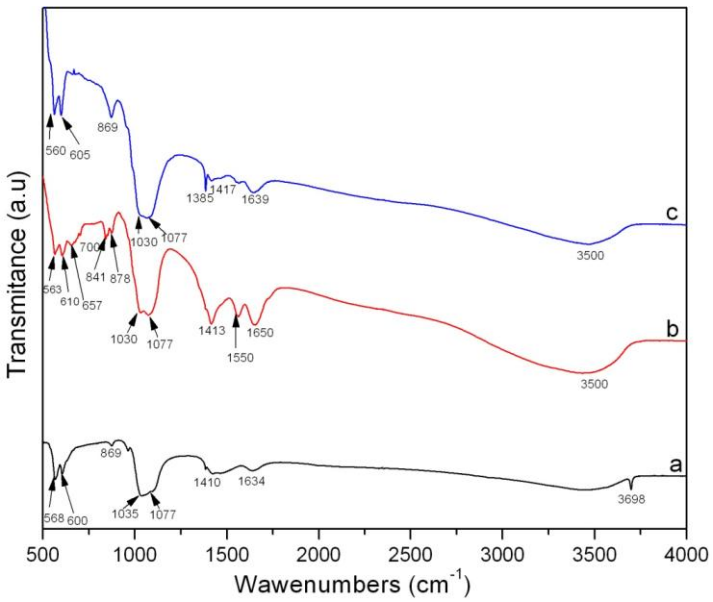

Fig. 4. FTIR spectra of untreated (synthesized) samples: a) CaMgP, b) CaP and c) CaSrNaP.

Furthermore, the FTIR spectrum of CaMgP shows a slight indication of 1410 cm^{-1} carbonate band (Fig. 4a) thus indicating no significant presence of CO_3 group in CaMgP powder [40]. Weak band of $MgHCO_3$ can be noticed around 1634 cm^{-1} [36]. CaSrNaP band at 1385 cm^{-1} indicates incorporation of Sr^{2+} and Na^{+} ions into the structure of hydroxylapatite (Fig. 4c) [35, 38]. A band that indicates carbonate group (coming from the reaction medium) in the structure of CaSrNaP is demonstrated by bands at 1417 and 1639 cm^{-1} [41]. FTIR spectra confirm previously described XRD results, that using acetate solution multi doped hydroxyapatite material can be obtained.

FTIR spectra of thermally treated samples at 1000 ºC for 3 h in air are shown in Fig. 5, also shows presence of the characteristic signals of apatite [36]. $CaMgP_{1000}$ (Fig. 5a) sample shows bands in spectral regions 1470-870 cm^{-1} and 605-560 cm^{-1} which are generally related to P-O species with different phosphorous configuration [42, 43]. Characteristic vibrations of $Mg_2P_2O_7$ phase are bands at 1050, 605 and 560 cm^{-1} [42]. The bands at around 1050 cm^{-1} belong to triply degenerate asymmetric P-O stretching mode, while the band around 955 cm^{-1} belongs to P-O stretching mode, these bands belong to β-$Ca_2P_2O_7$ phase [43]. There is no evidence of any characteristic hydroxyl group vibrations (631 and 3572 cm^{-1}). CaP_{1000} (Fig. 5b) bands are weaker than in untreated samples indicating lack of water vibrations in structure. The bands around 600 and 580 cm^{-1} are attributed to different types of P-O-P bending mode vibrations, which belong to β-$Ca_2P_2O_7$ [43]. Figure 5c shows vibration spectrum of $CaSrNaP_{1000}$ material. Presence of previously described P-O and P-O-P vibrations which belong to β-$Ca_2P_2O_7$ phase also belong to $Sr_2P_2O_7$ [43, 44]. The band around 740 cm^{-1} belongs to P-O-P bridge stretching vibration, a striking feature of $(P_2O_7)^{4-}$ ions in $Sr_2P_2O_7$. FTIR spectrum of CaSrNaP (Fig. 5c) shows no evidence of O-H stretching modes at around 3500 and 1600 cm^{-1} [44]. Metal-oxygen vibrations in these types of systems are generally too low to be seen in the 400-4000 cm^{-1} region.

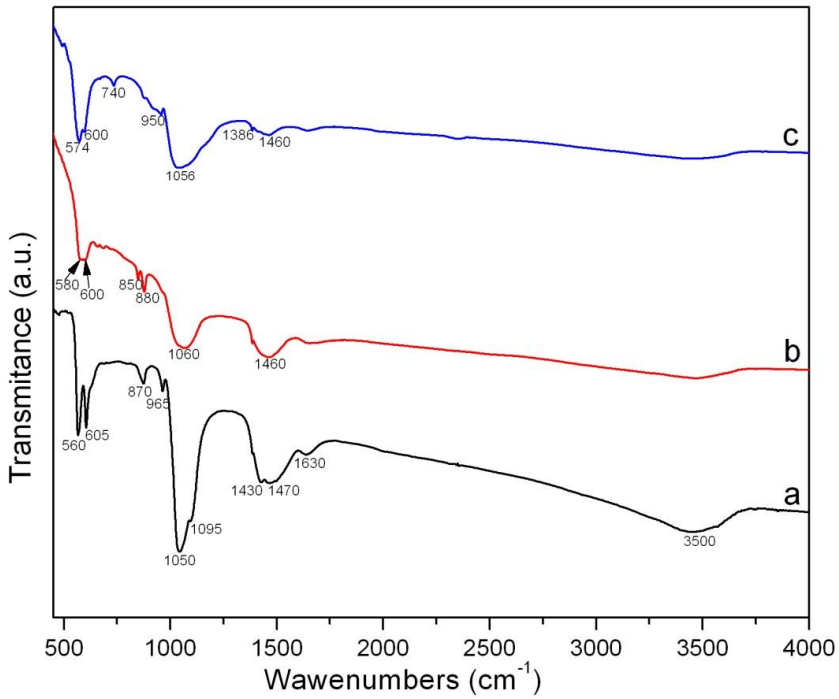

Fig. 5. FTIR specta of thermally treated samples at 1000 °C in air for 3 h: a) $CaMgP_{1000}$, b) CaP_{1000} and c) $CaSrNaP_{1000}$.

Based on FTIR analysis, at 1000 °C high temperature $CaMgP_{1000}$ material is obtained. All of identified vibrations that belong to CaP_{1000} material (Fig. 5b) confirm that β-$Ca_2P_2O_7$ is obtained by sintering hydroxyapatite for 3h on 1000°C in air atmosphere. The analysis of $CaSrNaP_{1000}$ spectrum (Fig. 5c) confirms absence of O-H vibrations and presence of $(P_2O_7)^{4-}$ vibrations which is unique for $X_2P_2O_7$ types of compounds [43, 44].

3.1.3. Morphology (SEM analysis) and element composition (EDS analysis)

SEM analysis confirms that all obtained samples using precipitation method have crystallite size of nanometer dimensions. In addition, SEM images (Fig. 6) show that the particle size in all samples increases with the increase of temperature. Namely, nanoparticles have a natural tendency to agglomerate for two reasons: firstly−the agglomeration is a more sTab. configuration from an energetic point of view, and secondly−the agglomeration allows the crystallite growth [45, 46].

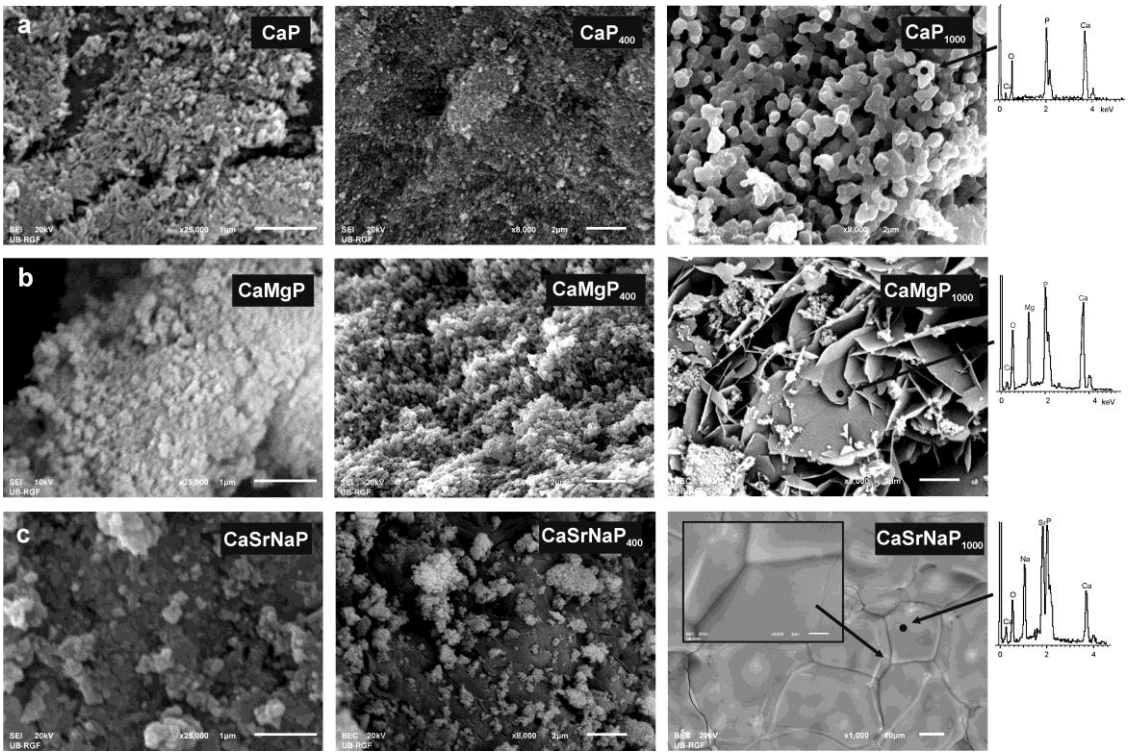

Fig. 6. SEM micrographs of A): CaP, CaP_{400} and CaP_{1000}; B) CaMgP, $CaMgP_{400}$ and $CaMgP_{1000}$; C) CaSrNaP, $CaSrNaP_{400}$ and $CaSrNaP_{1000}$; with EDS spectra.

Sintering at 1000 ºC in air for 3 h led to a higher degree of densification of $CaSrNaP_{1000}$ (98 % TD) than of $CaMgP_{1000}$ (86 % TD). The main reason for the differences in density may be pore and particle size distribution, i.e. different morphology (Fig. 6). The samples after calcinations at 400 ºC during 3 h show more uniform particles and well ordered structure. Calcinations was done in order to allow better packing and lower inner activity, and it was expected that these samples may achieve higher density after sintering. This was achieved for $CaSrNaP_{1000}$ sample, where the grains are uniformly sintered and the contacts between grains show hexagonal forms and the inserted section clearly demonstrates that we have indeed obtained dense high temperature CaSrNaP material (Fig. 6c). On the other hand, $CaMgP_{1000}$ (Fig. 6b) exhibits grain growth due to formation of agglomerated grains. Densification retards or inhibits wide pore distribution, during densification the big pores

became larger while small pores shrink and disappear [47, 48]. SEM micrograph of $CaMgP_{1000}$ (Fig. 6b) shows numerous agglomerates of hexagonal particles with plate like morphology bonded together, with average grain size between 2 and 5 μm with non-uniform particles with many vacancies, less compact particle packing, higher inner activity. To confirm the chemical composition, the EDS microanalysis was done on the CaP_{1000}, $CaMgP_{1000}$ and $CaSrNaP_{1000}$ sintered samples (Fig. 6). It revealed that chemical composition very similar to nominal chemical composition. According to semi quantitative chemical analysis, the mean values for the ratios Ca/P/O for CaP_{1000} sample determined from four runs are 2.1/2/7.5. These ratios correspond to empirically calculated compound with nominal composition-($Ca_{2.1}P_2O_{7.5}$). The mean value of the chemical ratios Ca/Mg/P/O for $CaMgP_{1000}$ was also determined from four runs, and amounts to 1.2/0.7/2/7, which corresponds to empirical compound with following composition-$(Ca_{1.2}Mg_{0.7})_{1.9}P_2O_7$. The mean value of the chemical ratios Ca/ Sr Na/ /P/O of the $NaSrHA_{1000}$ sample was determined from four runs, and amounts to 0.5/0.6/2/2/7, which corresponds to-$Ca_{0.5}Sr_{0.6}Na_2P_2O_7$. These results (Fig. 6) confirm the assumption that sintered samples based on hydroxyapatite at high temperature (1000 ºC) remain sTab. and almost nominal chemical composition. The obtained EDS results are in good agreement with XRD results.

3.2. Electrical conductivity

Recently, ionic conductors with the apatite type structures attracted a great deal of attention as an alternative electrolytes to the conventional yttria-stabilized zirconia to operate in IT–SOFCs, in the intermediate temperature range (600-800 ºC) [49-52]. Namely, hydroxyapatite belongs to apatitic group of phosphate minerals with general formula $Me_{10}(XO_4)_6Y_2$ with ionic substitution ability [53]. Based on XRD (Tab. I), unit cell parameters of CaMgP samples are slightly increased compared to pure CaP sample, the contraction of *a* and *c* parameter can be attributed to much smaller ionic radius of Mg^{2+} than Ca^{2+} [54]. The change of unit cell parameters *a* and *c* of CaSrNaP indicate that Sr^{2+} and Na^+ ions are incorporated in structure, and not just adhered to the crystal where Sr^{2+} will firstly replace Ca^{2+} ion in Ca2 site [55]. On the other hand Na^+ ion as a smaller than Ca^{2+} could possible replace Ca^{2+} in Ca1 site while a vacancy may formed at the OH^- site [56]. At 1000°C structural transformation of hydroxyapatite occurs and it transforms to a high temperature mixed phosphate ceramics with $M_2X_2O_7$ structure where X ions are tetrahedral coordinated (Fig. 7.)

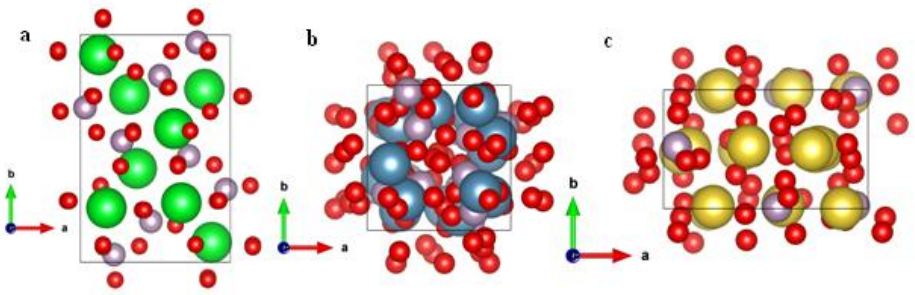

Fig. 7. Structures of $M_2X_2O_7$: a) α–$Sr_2P_2O_7$, b) β–$Ca_2P_2O_7$ and c) $Na_4P_2O_7$; (the green spheres are Sr atoms, blue spheres are Ca atoms, the yellow spheres are Na atoms, the red spheres are O atoms and the purple spheres are P atoms).

The crystal structures of calcium, strontium and sodium phosphate materials are comprised of diphosphate ions which are linked to metallic ions to form a three

dimensional network in β – $Ca_2P_2O_7$, α-$Sr_2P_2O_7$ and $Na_4P_2O_7$ structures [57, 58]. A common characteristic of thermal behavior of all phosphates is that under thermal treatment they undergo dehydratation-condensation reaction which leads to phosphate tetrahedral bonded to mutual oxygen atom. The ion conductivity in these materials occurs mainly via O^- interstitials with preferential *c*–axis conduction [50, 51, 56, 59] in comparison to O^{2-} vacancy migration in fluorite and perovskite–based electrolytes [59-63].

Generally, the impedance spectra are presented as negative of imaginary component of impedance ($-Z_{imag}$) versus real component of impedance (Z_{real}) i.e., as Nyquist plot. The semicircles at high and intermediate frequency are ascribed to bulk and grain boundary processes, respectively, while semicircle at low frequency represents the electrode process contribution [56]. In our case, for the potential application in IT-SOFCs the measurements of ionic conductivity of electrolytes in solid state of the $CaMgP_{1000}$ and $CaSrNaP_{1000}$ samples were done in intermediate temperature range of 500-700 ºC, with the increments of 50 ºC. The original Nyquist plots recorded in the available frequency range (1 Hz-100 kHz) are presented in Fig. 8. As it could be seen (Fig. 8a and 8b), with increasing the temperature the values of both resistance elements (R_b and R_{gb}) obviously decrease, which causes an increase in ω_{max}. Consequently, the whole region of the impedance points shifts towards the low–frequency semicircle and at higher temperatures, instead of R_b and R_{gb} separately, only the whole sum R_b+R_{gb} became readable in the available frequency range. In this case, at higher temperatures, the time constants associated with the bulk and grain boundary impedances are much lower than those associated with the electrode interface. As a result, semicircles due to bulk and grain boundary disappear and only a single semicircle due to electrode interfacial processes can be observed [64, 66]. Therefore, only the whole sum R_b+R_{ig} became readable and the values of total resistance were estimated from the experimental cross section of obtained semicircles with the real component of impedance (Z_{real}), this intercept is marked by arrows in Fig. 8 (inset). New semicircles are observed to appear in a low–frequency region, being particularly visible in temperature range at 650-700 ºC (Fig. 8b). Almost doubtless, it originates from the oxygen electrode reactions, O_2/O^{2-} [64], which does not belong to the scope of this study.

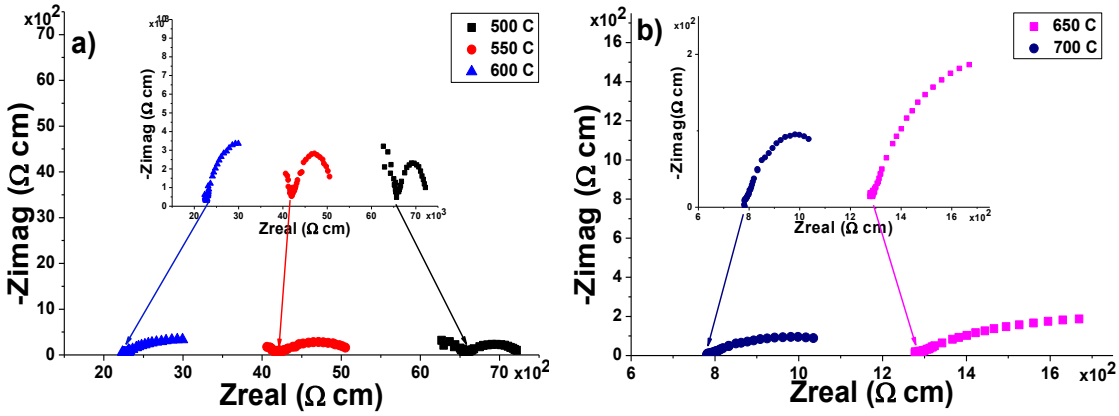

Fig. 8. (a)(b) Complex impedance plots of the sintered samples $CaSrNaP_{1000}$ measured in the temperature range from 500 to 700 ºC, in air atmosphere. The arrows indicate the points on the real axis corresponding to the readings R_b+R_{gb}.

The total ionic conductivity of the sintered $CaSrNaP_{1000}$ sample is shown in Tab. II. Obtained values (at 700 ºC amount to 4.18×10^{-3} $\Omega^{-1}cm^{-1}$) are slightly higher than previously published ones [64, 66]. More specifically, values of ionic conductivity observed at 700 ºC in this work,

are similar to values obtained at 800 and 900 ºC [67-71]. This holds also if we compare the results we found at lower temperatures with the literature data [64-67].

Tab. II The temperature dependence of total ionic conductivity (κ) of the sintered $CaMgP_{1000}$ and $CaSrNaP_{1000}$ sample.

COMPOSITION	κ $(\Omega^{-1}cm^{-1})$ ***500 ºC***	κ $(\Omega^{-1}cm^{-1})$ ***550 ºC***	κ $(\Omega^{-1}cm^{-1})$ ***600 ºC***	κ $(\Omega^{-1}cm^{-1})$ ***650 ºC***	κ $(\Omega^{-1}cm^{-1})$ ***700 ºC***
$CaMgP_{1000}$	1.23×10^{-4}	2.22×10^{-4}	3.58×10^{-4}	2.94×10^{-4}	3.12×10^{-4}
$CaSrNaP_{1000}$	2.27×10^{-4}	3.56×10^{-4}	6.57×10^{-4}	1.17×10^{-3}	1.90×10^{-3}

According to the results listed in Tab. II, the dependence *log κ = f(1/T)* of the sintered sample $CaSrNaP_{1000}$ is presented in Fig. 9. The activation energy of conductivity (E_a) was calculated from the Arrhenius plot according to the equation:

$$\ln(\sigma \cdot T) = \ln A - \frac{E_a}{k} \cdot \frac{1}{T} \quad (1)$$

where σ is the conductivity, T is the absolute temperature, A is the pre-exponential factor and k is the Boltzmann constant. Activation energy of total conductivity for sintered $CaSrNaP_{1000}$ sample is 0.31 eV. E_a values presented in our work are much lower than previously found [67, 68, 70, 71]. In addition, comparing the obtained values of E_a with activation energies of similar oxygen ion conductors containing dopants [71], obtained E_a values were significantly lower. We suggest that this is a consequence of well–ordered structure and better process ability of nanopowders obtained application method.

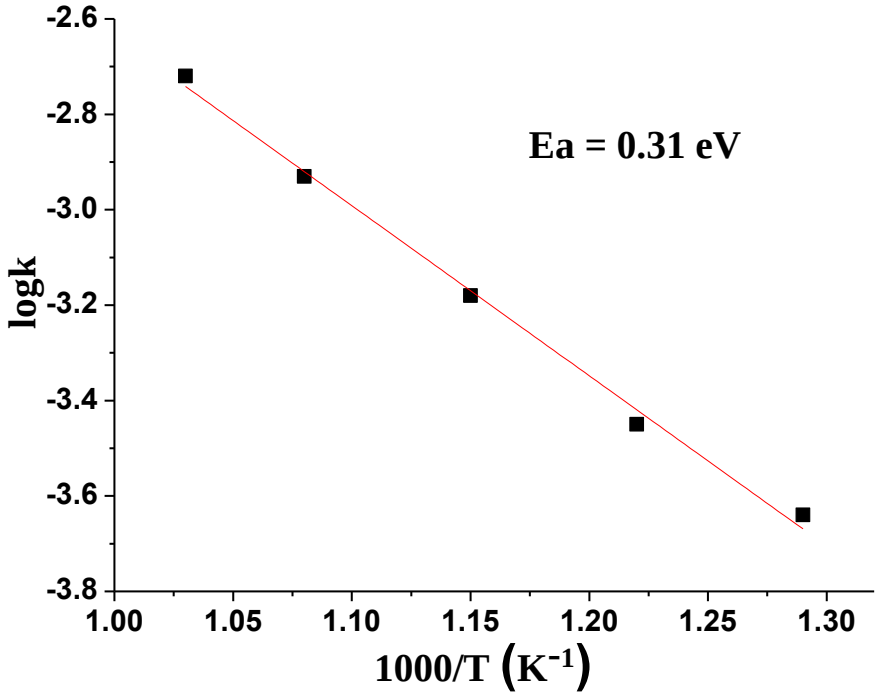

Fig. 9. The dependence *log κ = f(1/T)* of the sintered $CaSrNaP_{1000}$ sample.

4. Conclusions

The pure Ca and doped with Mg and NaSr hydroxyapatite (CaP, CaMgP and NaSrP) were successfully synthesized using slightly modified solution precipitation method (partial substitution nitrates by acetate solutions), and thus we achieved higher solubility and more cost effective synthesis. Any secondary phase that formed during synthesis decomposed during thermal treatment, leaving pure CaP, CaMgP and CaSrNaP hexagonal (*P63/m*) $Ca_5(PO_4)_3OH$ materials at room temperature. During sintering process at 1000 ºC in an air for 3 h, we developed high temperature doped calcium phosphate materials i.e. $CaMgP_{1000}$ and $CaSrNaP_{1000}$ materials. SEM analysis showed that $CaMgP_{1000}$ and $CaSrNaP_{1000}$ materials have high structural arrangement, EDS analysis confirmed that we obtained phosphate compound type-$M_2X_2O_7$. The fine crystalline powders after sintering at 1000 ºC achieved 98 % of theoretical density. The maximum value of electrical conductivity at 700 ºC was achieved for $CaSrNaP_{1000}$ material with amounts to 1.90×10^{-3} $\Omega^{-1}cm^{-1}$. Electrical characteristics of the sintered samples indicate the superiority of solid solution for the application in SOFCs. Additionally, considering high sintering temperature, one can conclude that the obtained phosphate material demonstrates high thermal stability, an important characteristics in its potential use as solid electrolyte. However, it is important to note that the future research should include furthering lower temperature synthesis routes, improving stability IT–SOFCs electrolyte/electrode, molecular dynamics (MD) simulations of conduction mechanisms and the general search for improved ion conductors. Also, the breadth of possible doping regimes in this phosphate material provides new opportunities to design and optimize their transport parameters for potential clean energy applications.

Acknowledgements

This work was supported by the Ministry of Education, Science and Technological development of Serbia as part of Projects: III 45012 and OI 176016.

5. References

1. A. V., Galvagno Chiodo, F. Urbani, F. Freni, Int. J. Hydrogen Energy., 38 (2013) 3913.
2. Y. Takagi, K. Kerman, C. Ko, S. Ramanathan, J. Power Sources., 243 (2013) 1.
3. H. J. Alves, C. Bley Junior, R. R. Niklevicz, E. P. Frigo, M. S. Frigo, C. H. Coimbra-Araújo, Int J. Hydrogen Energy., 38 (2013) 5215.
4. J-J. Liu, S-Q. Zhang, W.-D. Wang, J.-F. Gao, W. Liu, C.-S. Chen, J. Power Sources., 287 (2012) 287.
5. J. L. Hertz, H. L. Tuller, J. Electroceram., 13 (2004) 663.
6. S. J. Litzelman, J. L. Hertz, W. Jung, H. L. Tuller, Fuel Cells, 8 (2008) 294.
7. E.Y. Pikalova, A. A. Murashkina, V. I. Maragou, A. K. Demin, V. N. Strekalovsky, P. E. Tsiakaras, Int Journal Hydrogen Energy, 36 (2011) 6175.
8. D. Magdalena, Int. J. Electrochem. Sc., 7 (2012) 2874.
9. M. Stojmenović, S. Bošković, M. Žunić, B. Babić, B. Matović, D. Bajuk-Bogdanović, Mat. Chem. Phys., 153 (2015) 422.
10. M. Stojmenović, M. Žunić, J. Gulicovski, D. Bajuk-Bogdanović, I. Holclajtner-Antunović, V. Dodevski, J. Mater. Sci., 50 (2015) 3781.
11. A. Laghzizil, N. Elherch, A. Bouhaouss, G. Lorente, T. Coradin, J. Livage, Mater. Res. Bull., 36 (2001) 953.

12. K. Yamashita, H. Owada, T. Umegaki, T. Kanazawa, T. Futagami, Solid State Ionics, 28 (1988) 660.
13. F. Bakan, O. Laçin, H. Sarac, Powder Technol., 233 (2013) 295.
14. M. Sadat-Shojai, M-T. Khorasani, A. Jamshidi, J Cryst Growth, 361 (2012) 73.
15. S. Pramanik, A. K. Agarwal, K. N. Rai, A. Garg, Ceram. Int., 33 (2007) 419.
16. I. Mobasherpour, M.S. Heshajin, A. Kazemzadeh, M. Zakeri, J. Alloys. Comp., 430 (2007) 330.
17. A. K. Nayak, Int. Jour. Chem.Tech. Res., 2 (2010) 903.
18. T. T. Trang Pham, T. Phuong Nguyen, T. Nam Pham, T. Phuong Vu, D. L. Tran, H.Thai, Vietnam Academy of Science and Technology, 4 (2013) 1.
19. S. C. Cox, P. Jamshidi, L. M. Grover, K. K. Mallick, Mat. Sci. Eng C-Bio S., 35 (2014) 106.
20. E. Champion, Acta Biomater, 9 (2013) 5855.
21. S. J. Kalita, A. Bhardwaj, H. A. Bhatt, Mat. Sci. Eng C-Bio S., 27 (2007) 441.
22. S. Ramesh, K. L. Aw, R. Tolouei, M. Amiriyan, C. Y. Tan, M. Hamdi, Ceram. Int., 39 (2013) 111.
23. Đ. Veljović, G. Vuković, I. Steins, E. Palcevskis, P. S. Uskoković, R. Petrović, Sci. Sinter., 45 (2013) 233.
24. S. Raynaud, E. Champion, D. Bernache-Assollant, Biomater., 23 (2002) 1073.
25. Rigaku Corporation, Tokyo J. PDXL Version 2.0.3.0 Integrated X-ray Powder Diffraction Software. 2011.
26. Powder Diffraction File P-D, announcement of new data-base release 2012, International Centrefor Diffraction Data (ICDD).
27. K. Momma, F. Izumi, J. Appl. Crystallogr., 44 (2011) 1272.
28. M. Prekajski, M. Mirković, B. Todorović, A. Matković, M. Marinović-Cincović, J. Luković, B. Matović, J. Eur. Ceram.Soc., 36 (2016) 1293.
29. J. Wang, L.L. Shaw., Adv. Mater., 19 (2007) 2364.
30. A. Mortier, J. Lemaitre, P. Rouxet, Thermochim. Acta., 113 (1987) 133.
31. R. T. Downs, M. Hall-Wallace, Am. Mineralog., 88 (2003) 247.
32. G. Qi, S. Zhang, K. A. Khor, C. Liu, X. Zeng, W. Weng, Thin Solid Films, 516 (2008) 5176.
33. S. C. Cox, P. Jamshidi, L. M. Grover, K. K. Mallick, Mat. Sci. Eng C-Bio S., 35 (2014) 106.
34. A. Cuccu, S. Montinaro, R. Orrù, G. Cao, D. Bellucci, A. Sola, Ceram. Int., 41 (2015)725.
35. W. Zhang, Y. Shen, H. Pan, K. Lin, X. Liu, B. W. Darvell, Acta Biomater., 7 (2011) 800.
36. J. A. Gadsden. Infrared spectra of minerals and related inorganic compounds: Butterworths, London; 1975.
37. M. Iafisco, A. Ruffini, A. Adamiano, S. Sprio, A. Tampieri, Mat. Sci. Eng C-Bio S., 35 (2014) 212.
38. S. Koutsopoulos,. J. Biomed. Mater. Res., 62 (2002) 600.
39. S-C. Liou, S-Y. Chen, H-Y. Lee, J-S. Bow, Biomaterials., 25 (2004) 189.
40. M. E. Fleet, Biomaterials., 30 (2009) 1473.
41. N. V. Chukanov, Infrared spectra of mineral species: Extended library: Springer London, Limited; 2013.
42. V. Koleva, V. Stefov, M. Najdoski, A. Cahil, Thermochim. Acta., 619 (2015) 20.
43. B. Mehdikhani, G. H. Borhani, J. Ceram. Process. Res., 16 (2015) 308.
44. P. Solanki, S. Vasant, M. Joshi, Int. J. Appl. Ceram. Tech., 11 (2014) 663.
45. G. B. Balazs, R. . Glass, Solid State Ionics., 76 (1995) 155.
46. G. Buvaneswari, K. Valsalan, Mater. Lett., 134 (2014) 252.

47. A. Farzadi, F. Bakhshi, M. Solati-Hashjin, M. Asadi-Eydivand, N. A. Osman, Ceram. Int.,40 (2014) 6021.
48. A. G. Evans, C. H. Hsueh, J. Am. Ceram. Soc., 69 (1986) 444.
49. A. J. Jacobson, Chem. Mater., 22 (2010) 660.
50. A. Orera, P. R. Slater, Chem. Mater., 22 (2010) 675.
51. L. Malavasi, C. A. J. Fisher, M. S. Islam, Chem. Soc. Review., 39 (2010) 4370.
52. D. Marrero-López, M. C. Martín-Sedeño, J. Peña-Martínez, J. C. Ruiz-Morales, P. Núñez, M. A. G. Aranda, J. Power Sources., 195 (2010) 2496.
53. M. P. Moreira, G. D. de Almeida Soares, J. Dentzer, K. Anselme, L. Á. de Sena, A Kuznetsov, Mat. Sci. Eng C-Bio S., 61 (2016) 736.
54. F. Ren, Y. Leng, R. Xin, X. Ge, Acta Biomater., 6 (2010) 2787.
55. Z. Y. Li, W. M. Lam, C. Yang, B. Xu, G. X. Ni, S. A. Abbah, Biomaterials., 28 (2007)1452.
56. Z. Leilei, L. Hejun, L. Kezhi, F. Qiangang, Z. Yulei, L. Shoujie, Ceram. Int., 40 (2014) 13123.
57. K. Y. Leung, C. Calvo, Can. J. Chem., 50 (1972) 2519.
58. H. Larsove, J. Ingela, M. Christina, Acta Chemica Scandinavica., 22 (1968) 1419.
59. E. Kendrick, M. S. Islam, P. R. Slater, J. Mater. Chem., 17 (2007) 3104.
60. E. Kendrick, M. S. Islam, P. R. Slater, Chem. Commun., 715 (2008) 7.
61. K. Fukuda, T. Asaka, R. Hamaguchi, T. Suzuki, H. Oka, A. Berghout, Chem. Mater., 23 (2011) 5474.
62. E. Kendrick, M. S. Islam, P. R. Slater, Solid State Ionics., 177 (2007) 3411.
63. L. Leon-Reina, E. R. Losilla, M. Martinez-Lara, S. Bruque, M. A. G., J. Mater. Chem., 14 (2004) 1142.
64. N. Nallamuthu, I. Prakash, N. Satyanarayana, M. Venkateswarlu, J. Alloys and Compounds, 509 (2011) 1138.
65. M. Sato, Y. Kono, H. Ueda, K Uematsu, K Toda, Solid State Ionics, 83 (1996)249.
66. D. Marrero-López, L. dos Santos-Gómez, L. León-Reina, J. Canales-Vázquez, E. R. Losilla, Journal of Power Sources., 245 (2014) 107.
67. S. Nakayama, T. Kageyama, H. Aono, Y. Sadaoka, J. Mater. Chem., 5 (1995) 1801.
68. Y. Masubuchi, M. Higuchi, T. Takeda, S. Kikkawa, J. Alloys and Compounds, 408 (2006) 641.
69. J. McFarlane, S. Barth, M. Swaffer, J. E. H. Sansom, P. R. Slater, Ionics, 8 (2002) 149.
70. S. Tao, J. T. S. Irvine, Mater. Res.Bullet., 36 (2001) 1245.
71. J. E. H. Sansom, J. R. Tolchard, P. R. Slater, M. S. Islam, Solid State Ionics., 167 (2004) 17.

Садржај: *Метода таложне титрације коришћена је за добијање чистог и допираног хидроксиапатита јонима Sr, Mg и Na (CaP, CaMgP and CaSrNaP). За синтезу супституисаних хидроксиапатитских материјала коришћена је модификована таложна метода у односу на досада познате методе. Због боље растворљивости и знатно веће исплативости коришћени су раствори ацетата уместо нитрата. Синтетисани материјали су калцинисани на 400 °C, а затим окарактерисани рендгенском дифракцијом, инфра црвеном спектроскопијом са Фуријеовом трансформацијом и скенирајућом електронском микроскопијом. Калцинисани узорци су синтеровани на 1000 °C са задржавањем од 3 сата у атмосфери ваздуха (CaP_{1000}, $CaMgP_{1000}$ and $CaSrNaP_{1000}$). Синтеровани материјали окарактерисани су: рендгенском дифракцијом на поликристалном узорку, инфрацрвеном спекторскопијом са Фуријеовом трансформацијом и скенирајућом електронском микроскопијом са*

енергетско дисперзивном анализом као и методе комплексне импендансе. Највећа проводљивост добијена је на температури од 700 °C и износи $1.90\times^{10\text{-}3}$ $\Omega^{-1}cm^{-1}$ *за мешовито допирани фосфатни материјал* ($CaSrNaP_{1000}$). *Добијене активационе енергије проводљивости износе 0.31 eV у температурном опсегу од 500-700 ºC.*

Кључне речи: *Синтеровање, Рендгенска дифракција, Електрична проводљивост, Фосфатни материјали, Горивне ћелије.*